Accepted manuscript

https://doi.org/10.1016/j.electacta.2022.140872

***Electrochimica Acta* 427: 140872.**

Deepening into the charge storage mechanisms and electrochemical performance of TiO_2 hollandite for sodium-ion batteries

Angélica Duarte[a], Pilar Díaz-Carrasco [a], Alois Kuhn[a] , Anna Basa[b] and Flaviano García-Alvarado[a,*]

[a] *Departamento de Química y Bioquímica, Facultad de Farmacia, Universidad San Pablo-CEU, CEU Universities, Urbanización Montepríncipe, 28668 Boadilla del Monte, Madrid, Spain*

[b] *Faculty of Chemistry, University of Białystok, K. Ciolkowskiego 1K, 15-245 Białystok, Poland*

* corresponding author: **flaga@ceu.es**

Keywords: hollandite TiO_2; sodium ion negative electrode; sodium diffusion coefficient; high-capacity anode; sodium ion battery

Abstract

The electrochemical performance of TiO_2 hollandite, TiO_2(H), obtained by complete K^+ ion extraction of the bronze $K_{0.2}TiO_2$ is investigated. TiO_2 develops a fairly stable capacity of 106 mAh g^{-1} after 300 cycles at C/8 (42 mA g^{-1}) and maintains 100 mAh g^{-1} after 600 cycles. At high current rate (2C, 671 mA g^{-1}) 55 mAh g^{-1} is still maintained. Cycling produces nanosizing of the TiO_2 electrode (to 200-300 nm) by electrochemical milling but cyclic voltammetry at different sweep rates indicates that diffusive controlled faradic contribution to the total capacity of TiO_2(H) due to Na insertion is significant even at high current. However, participation of pseudocapacitive charge storage is unveiled. The voltage profile resembles in fact that of pseudocapacitive materials with no clear evidence of a constant voltage region. *Operando* XRD confirmed the lowering of symmetry from tetragonal *I*4/*m* to monoclinic *I*2/*m* upon sodiation with a relatively narrow two-phase region different from other long plateaus of typical battery materials. Cyclic voltammetry clearly indicates that the two peaks (centered at 1.25 and 0.5 V on reduction) correspond to diffusion-limited faradic processes. Thus, it can be said that hollandite TiO_2 is a battery-like material, but for which kinetics is not limited by a biphasic transformation. Instead, kinetics is limited mainly by slow diffusion in single phases with variable composition (continuous variation of voltage vs. capacity) that are formed upon Na^+ intercalation into the tunnels. The limited diffusion at high sweep rate favors the dominance of pseudocapacitance (charge transfer at the surface). A comparison with the bronze $K_{0.2}TiO_2$ reveals the importance of potassium in the electrochemical properties and the nature of the different physicochemical processes of both compounds.

Sodium ion diffusion coefficient in TiO_2(H), $2.6 \cdot 10^{-13}$ cm^2 s^{-1}, is several orders of magnitude higher than that of TiO_2 rutile and anatase, however it does not provide a fast intercalation into the tunnels to consider it a pseudocapacitive intercalation material.

1. Introduction

Na-ion batteries (SIBs) have become a focus of research in energy storage for large-scale stationary applications because of their low cost when compared with lithium analogous technologies. As in the case of lithium-ion batteries (LIBs), carbonaceous materials fulfil many of the requirements to be used as the negative electrode. Thus, if insertion of lithium in graphitic carbon has been for years the state-of-the-art lithium-ion anode material, hard carbons are among the most appropriate materials for the anode of sodium-ion batteries. For LIBs, due to safety issues (plating and dendritic growth) other materials with higher intercalation voltage and excellent structural stability upon cycling, the so called zero strain or near-zero volume change anodes, were investigated.[1-4] Thus, $Li_4Ti_5O_{12}$ also reached the market of lithium-ion batteries. The parallelism of lithium and sodium hosts becomes apparent, because $Li_4Ti_5O_{12}$ can intercalate significant amounts of sodium delivering 155 mAh g^{-1} at 0.9 V vs. Na^+/Na paralleling also the zero-strain behavior.[5, 6]

Lithium insertion in hollandite-type bronzes $K_xTi_8O_{16}{\cdot}n\ H_2O$ ($1.65 \leq x \leq 0.03$) was first reported by Gutiérrez et al. [7, 8], evidencing that ability for Li storage greatly depends on the amount of potassium ions in the tunnel space. The sample with the lowest potassium content $K_{0.03}Ti_8O_{16}$ (when referred to the unit cell, Z=1 or $K_{0.004}TiO_2$, Z=8, when referred to one formula unit TiO_2), was considered as practically potassium-free, and these authors reported enhanced intercalation of lithium in hollandite-type TiO_2 for the first time.[8] Interestingly, the potassium-free sample exhibited a high capacity of 260 mAh g^{-1}, this is 77% of the theoretical capacity (336 mAh g^{-1} corresponding to 1 electron transfer, reduction of 1 Ti^{4+} to Ti^{3+}). K-free TiO_2 showed significant polarization, while samples with higher potassium content showed little polarization albeit low capacity, revealing that residual potassium ions in the hollandite tunnel space are crucial for the electrochemical performance in lithium cells. In fact, lithium diffusion coefficient of $K_{0.06}TiO_2$ hollandite is 2.29 $\cdot 10^{-10}$ cm^2 s^{-1} whereas for a larger amount of

potassium such as $K_{0.15}TiO_2$ this coefficient is four orders of magnitude lower [9]. The presence of K^+ ions, on the contrary, linked to partial reduction of Ti^{4+} to Ti^{3+} favors electronic conductivity. For instance, reversible capacity in $K_{0.022}TiO_2$ is less than 200 mAh g^{-1}, which represents a decrease of more than 20% when compared to K-free TiO_2. In line with this, Noailles et al. [10] reported poor electrochemical lithium insertion properties of a K^+-extracted K_xTiO_2 in the 1-2 V range, despite a relatively high initial capacity of 160 mAh g^{-1}, attributable to residual K^+ ions in the (2 × 2) tunnels which would impede Li insertion. In contrast, a significant capacity, ca. 160 mAh g^{-1}, of a sample with an essentially empty tunnel ($K_{0.008}TiO_2$) was reported by Sakao et al. [11, 12] with good retention of capacity and crystalline structure. On the other hand, while K_xTiO_2 bronzes exhibit well-defined voltage drops and plateaus pointing to well-defined crystallographic sites being occupied by lithium during the formation of different single phases, the potassium-free TiO_2 exhibits a featureless continuously decreasing voltage profile [8] This could be indicative of a more disordered situation for lithium ions producing a solid solution.

Other titanium oxides have also been investigated for LIBs due to their very high theoretical capacities (336 mAh g^{-1}), reaching high-performance lithium insertion in different topologies (for instance anatase [13], rutile [14-16], hollandite [8], ramsdellite [17], brookite [18] and TiO_2 (B) [19]. In the case of nano-sized rutile TiO_2, reaction with lithium produces a new electroactive phase that sustains high reversible capacity and whose reaction mechanism and origin of high performance has been recently unveiled. [20]

Some titanium oxide polymorphs are also able to insert or to react with sodium and they have aroused high interest as negative electrodes for low-cost sodium ion batteries. [21] Nevertheless, nanosizing and proper processing is usually needed: anatase [22, 23] that delivers only 38 mAh g^{-1} at 10C but increases to 104 mAh g^{-1} when coated with carbon; rutile that needs to be doped in order to enable intercalation [24] (160 mAh g^{-1} at cycle 50); nano TiO_2 (B) [25] (ca. 80 mAh g^{-1} at 50 mA g^{-1}). However, the most stable 3-D polymorphs with smaller structural cavities are likely to undergo structural stress upon reaction with sodium or to induce sluggish

sodium ion diffusion. Fig. S1 of SI shows the schematic representation of Ti and O atomic arrangements in rutile, anatase TiO_2 (B) and hollandite structures. Owing to the bigger size of Na^+ ion when compared to Li^+ ($r(Na^+)$ = 1.02 Å vs. $r(Li^+)$ = 0.76 Å for c.n.=VI) [26], the most appropriate candidate for intercalation reactions seems to be TiO_2 hollandite with larger tunnel spaces. The length of the diagonal O-O distance of rhombic or square oxygen windows gives an idea of how "open" a structure is. Hollandite with the longest O-O distance (6.9 Å) and the lowest density (3.46 g cm^{-3}) among the four selected TiO_2 modifications has hence the more open structure.

Pérez-Flores et al. [27] reported that an almost potassium-free hollandite $K_{0.023}TiO_2$ exhibits a very large first discharge capacity (280 mAh g^{-1}) which drops to 85 mAh g^{-1} in the following cycles. In that study, electrodes made from pelletized mixtures of active material, conductive carbon and PVDF in a 65:30:5 weight ratio were used. *Operando* synchrotron X-ray diffraction showed that the tetragonal symmetry *I*4/*m* of Na_xTiO_2 is kept for x=0-0.17, while a reversible phase transition from tetragonal *I*4/*m* to monoclinic *I*2/*m* is observed with progressive Na uptake up to the end composition $Na_{0.25}TiO_2$(H) corresponding to 2 Na^+ per unit cell ($Na_2Ti_8O_{16}$). [27] The experimentally observed phase transition and the upper composition $Na_{0.25}TiO_2$ was later theoretically confirmed. [28] It seems that TiO_2(H) is the only one polymorph able to insert sodium developing sustainable significant capacities without nanosizing or further processing.

An interesting case regarding improvement by nanosizing is the bronze $K_{0.23}TiO_2$ reported by Q. Zhang et al.[29]. The nanorods prepared by in situ carbothermal reduction sustain a capacity of 131 mAh g^{-1} keeping 100 mAh g^{-1} after 1000 cycles at 1.7 C. This finding is unexpected if one considers that typically higher K content is associated with lower lithium storage capacity, [8] and the same would be expected for sodium insertion. However, note that the nature of the physicochemical processes responsible of charge storage can be different depending on particle size, morphology, and guest ion. Therefore, identification of such behavior and the materials that exhibit both capacitive and diffusion controlled charge storage have been pointed out to be critical. [30]

In view of the influence that residual potassium has on the electrochemical lithium insertion properties and that this would be also the case for sodium, in the present work we have investigated a potassium-free TiO_2 sample to deepen further into the electrochemical performance and the physicochemical charge storage processes. For this, we have determined the Na^+ diffusion coefficient at the dilute conditions and analyzed three different electrochemical features that characterize different electrochemical storage materials as well as the structural transformations related to the voltage-capacity profile. Finally, we have quantified the contribution of diffusive and capacitive (pseudocapacitive) processes to the total capacity at different sweep rates.

2. Experimental

A two-step process was used to obtain potassium-free TiO_2 hollandite using a cost-effective procedure. In a first step, bronze $K_{0.2}TiO_2$ [31] was synthesized by heating a stoichiometric mixture of K_2CO_3 and TiO_2 anatase at 950ºC for 8 h under a 5% H_2/Ar atmosphere. The resulting bronze was further ball milled for 1 h at 250 rpm to reduce particle size enabling faster oxidative K^+ ion extraction in the second step, which consisted in an oxidation using acidic H_2O_2 solution, similar to previous reports. [32] In a typical experiment 2 g of $K_{0.2}TiO_2$ were treated once with a mixture of 4 mL H_2O_2 (30% w/v) and 2 mL H_2SO_4 (98%) at 80º C for 24 h. Excess acid was afterwards removed by repeatedly washing with water (miliQ quality) and the solid was dried at 60 ºC.

For structural characterization, X-ray diffraction patterns were recorded on a Bruker D8 high-resolution diffractometer using CuKα radiation (λ = 1.5418 Å) and equipped with a LynxEye® solid-state position sensitive detector. Diffraction patterns of $K_{0.2}TiO_2$ bronze and oxidation product TiO_2 were analyzed and crystal structures determined by the Rietveld method using the FullProf program. [33]

For powder X-ray diffraction in *operando* conditions, a commercialized electrochemical cell akin to Leriche's cell, [34], fitted to the Bruker D8 diffractometer and equipped with CuKα radiation (λ = 1.5418 Å) was used. Discharge-charge experiments were run under a C/50 regime (1 Na^+ intercalated in 50 hours) in the 3.0 – 0.01 V vs. Na^+/Na voltage range. A thin circular Be foil was used as both the positive electrode current collector and transparent window for X-rays. Diffraction patterns were collected in the 10-80º 2θ range throughout a full electrochemical cycle. The time of data adquisition was 30 min per pattern. *Operando* XRD patterns were analyzed with LeBail profile fitting using Fullprof software.[33]

Morphological characterization of the hollandite precursor, oxidation product, and post-mortem electrodes was made by Scanning Electron Microscopy (SEM) using a FEI inspect S50 microscope. EDS was used to determine residual potassium content after oxidation. TEM images were taken using a FEI Tecnai T20 G2 X-Twin 200kV microscope.

For electrochemical characterization, positive electrodes were prepared from slurries composed of 62 wt % TiO_2(H), 28 wt % Super S carbon black (Cabot corp.) and 10% carboxymethyl cellulose as the binder (CMC) elaborated from distilled water. This slurry composition was selected because lower amount of carbon black as for instance 80:10:10 yielded 50% lower capacities. For comparison, the same ratio was used for the slurry bearing the bronze with nominal composition $K_{0.2}TiO_2$ as the active material.

Slurries were uniformly coated onto bare copper foils and then dried under vacuum at 80°C overnight. Finally, casted electrodes were punched into circular disks having 12 mm diameter and typical hollandite mass loading of 1.7 and 1.2 mg cm^{-2} for TiO_2(H) and $K_{0.2}TiO_2$, respectively. The electrolyte was 1 M $NaClO_4$ in EC:PC (1:1 vol %) and Whatman GF/D glass fiber was used as a separator. A sodium metal disc was used as the negative electrode. CR2032 coin cell assembly was performed in an argon-filled glove box (H_2O and O_2 content < 0.1 ppm). Galvanostatic discharge/charge

measurements were evaluated at 25ºC in the 3-0.01 V vs Na^+/Na voltage range at different constant currents from C/20 (17 mA g^{-1}) to 2C (671 mA g^{-1}). Cyclic voltammetry (CV) studies were carried out at 25ºC using a VMP3 system (BioLogic) at several scan rates from 1.2 mV s^{-1} to 0.03mV s^{-1} in the 2.5-0.01 V vs Na^+/Na voltage window.

Sodium diffusion coefficient of pristine TiO_2(H) at OCV conditions was calculated under the condition of semi-infinite diffusion by [35, 36]:

$$D = \left(\frac{V_M}{Z\,F\,A}\right)^2 \left(\frac{\Delta E}{\Delta x}\right)^2 \left(\frac{1}{m\,A_W\sqrt{2}}\right)^2 \qquad Eq.1$$

V_M is the molar volume, Z the number of electrons per inserted ion, F the Faraday constant, m the mass of the active material, and A the specific surface area of the electrode. The latter was determined by BET experiments (Micromeritics ASAP 2020 analyzer). The value of $\left(\frac{\Delta E}{\Delta x}\right)$ was determined from an initial slope of the E-x curve obtained from a galvanostatic intermittent titration experiment.

Impedance spectroscopy was used to determine the Warburg coefficient (A_w). Measurements were performed at open circuit voltage condition in a two-electrode cell. A three-electrode cell was used to determine the contribution of the anode to total impedance at low frequency to validate the higher quality data obtained from the two electrode cells for determination of the Warburg coefficient. Na metal discs were allocated at both the counter and the reference electrodes. Measurements were carried out at room temperature using a Biologic VMP3 galvanostat-potentiostat with an Electrochemical Impedance Spectroscopy channel. Equivalent circuit modelling was made using the Z-Fit (EC-lab® software). A sinusoidal potential perturbation of 10 mV was applied while measuring impedance variation at room temperature in the frequency range from $3 \cdot 10^5$ Hz to 0.1 Hz.

3. Results and discussion

3.1 Synthesis and characterization

Synthesis conditions allowed to obtain a completely potassium-free sample since no remaining potassium was detected by EDS. Fig. S2 of SI shows the XRD patterns of the $K_{0.20}TiO_2$ sample before and after potassium extraction. The XRD data confirmed that both parent $K_{0.20}TiO_2$ bronze and K^+-extracted TiO_2 were single-phase materials with the hollandite-type structure. $K_{0.20}TiO_2$ powders were bluish black before potassium extraction and changed to white after acid treatment in H_2O_2. All the diffraction peaks in the XRD patterns could be indexed using tetragonal symmetry with space group *I*4/*m*. The most relevant refined structural parameters are summarized in Tables S1 and S2 of SI. Refinement of occupancy factor of potassium in K_xTiO_2 yielded a slightly lower potassium content of x = 0.17 when compared to nominal x = 0.20, which is explained by loss of some potassium during the high-temperature treatment under reducing atmosphere. Reliable refinement of structure parameters of K on the commonly described non-splitted 2*a* (0 0 ½) position was obtained. [11, 12] . No attempts were made to adopt a split-atom model placing K on 4*e* (0 0 *x*) site as performed in previous reports. [37] For the K^+-extracted hollandite sample, no reliable structure refinement was obtained considering presence of some residual K yielding unreasonable thermal displacement factors and negative occupancies for potassium. We therefore assume that the oxidized compound is indeed the K^+-free TiO_2 hollandite, in agreement with results from EDS. The white color of the sample and absence of potassium point to the presence of only Ti^{4+}. Noteworthy, samples with even very small amount of potassium are pale gray as for instance $K_{0.023}TiO_2$. [27] The specific surface area is 6.98 ± 0.06 $m^2\ g^{-1}$ as determined from BET. Potassium can also be fully extracted using stronger oxidants, as for instance aqua regia. [11] However, we noticed that prolonged reaction with aqua regia produces a non-topotactical reaction, in which potassium-free hollandite fully transforms to nano-sized rutile. [20] Both $K_{0.20}TiO_2$ bronze and potassium-extracted TiO_2(H) are composed of microsized rods, and the topotactical K^+ extraction does change neither

morphology nor particle size as evidenced from SEM images shown in Fig. S3 of SI. TEM images in Fig. 1a and 1b further reveal that the rods were uniform in length (1-2 μm) and width (0.5 μm). Detailed analysis by HRTEM in Fig. 1c and 1d shows that the ordered lattice fringes with spacings of 0.72 nm and 0.29 nm, respectively, coincide with the (110) and (001) planes of $K_{0.20}TiO_2$ and TiO_2(H), suggesting that high crystallization of the product is maintained after complete removal of K^+.

3.2 Electrochemical properties

A discharge-charge profile plot corresponding to the first three cycles and cycles no. 50 and 300 of a galvanostatic run (C/8, 42 mA g^{-1}) of a cell bearing, TiO_2(H), the K^+-free hollandite, as the active material is shown in Fig. 2a. As indicated in the experimental section, the slurry composition (62:28:10) was used instead of the standard 80:10:10 to avoid high polarization due to the insulating character of TiO_2 and to achieve better electrical contact between micrometric big particles. The use of high amount of conductive carbon in related materials is not unusual [27, 38-42]. The variation of discharge and charge capacity during 600 cycles is shown in Fig. 2b together with coulombic efficiency. A high first discharge capacity of ca. 247 mAh g^{-1} is developed. Below ca. 0.45 V vs. Na^+/Na SEI formation has a significant contribution to this high initial capacity [27]. After SEI formation capacity drops to 117 mAh g^{-1} in the second cycle. Interestingly, capacity increases in the next 12 cycles reaching 133 mAh g^{-1} (0.4 Na^+/formula unit), as seen in Fig. 2b. This increase is due to the occurrence of electrochemical milling, as clearly seen in Fig. 3 which demonstrates the effect electrochemical milling has on morphology and size of TiO_2(H) particles. As-prepared TiO_2(H) is composed of micrometric irregular particles, as observed in Fig. S3 of SI and also shown casted on the current collector in Fig. 3a. Postmortem SEM image of the electrode after 100 cycles at C/20 (Fig. 3b) reveals a granular morphology with much smaller, more homogenously distributed particles (200-300 nm). In addition, the submicrometric particles are more loosely held together anticipating a poorer contact. Thus, electrochemical milling has two distinct effects: i) smaller particles are

beneficial because they enhance full sodiation by reducing diffusion length (capacity increases in the first cycles); ii) a looser distribution of particles has a detrimental effect, since more particles may become electrically disconnected (capacity decreases as polarization may increase). The slight decrease of capacity observed upon long cycling (Fig. 2b) can also be due to a non-optimized electrode processing and to an increasing cell resistance upon aging. However, capacity retention is quite acceptable. Note that upon long cycling, a fairly stable capacity is kept; from cycle 300 to 600 only a 5.5% capacity loss is observed and 100% coulombic efficiency is maintained. pointing to stability of both hollandite structure and SEI. Our findings represent an improvement of capacity by up to 60% with respect to previous reports [27] attributable to the complete absence of K^+ ions in the tunnel space whose presence hinders Na^+ intercalation. For comparison, Fig. S4 of SI shows the voltage-capacity profile for selected cycles (1-4 and 50), and the long cycling behavior at C/8 of parent bronze with nominal composition $K_{0.2}TiO_2$. The reversible capacity in the first few cycles is 80 mAh g^{-1}, compared with 133 mAh g^{-1} for TiO_2(H), and decreases to 63 mAh g^{-1} after 184 cycles proving that the micrometric bronze exhibits a limited electrochemical behavior. Since the presence of Ti^{3+} in bronze $K_{0.2}TiO_2$ makes the compounds electrically conductive, the increase of capacity due to electrochemical milling is not observed, and only minor changes in polarization are expected.

As far as discharge and charge capacity retention of TiO_2(H) at different current rates is concerned (Fig. 4), it holds a discharge and charge capacity of 105 mAh g^{-1} at medium current rate (C/8 or 42 mA g^{-1}). At high current (2C or 671 mA g^{-1}) 52% of capacity, 55 mAh g^{-1}, are kept, while a capacity of 120 mAh g^{-1} is recovered after returning to lower current (C/20 or 17 mA g^{-1}). The decrease of capacity with increasing current rate indicates that charge storage in hollandite TiO_2 is mainly due to a faradic process that becomes more impeded at high current due to limited mass diffusion throughout the bulk. However, the still high capacity observed at high current indicates that other physicochemical processes may be contributing to charge storage and therefore deserves further attention.

No other potassium-free TiO_2 hollandite has been reported to develop such good performance. However, similar performance has been reported for 50-100 nm diameter

nanorods of a bronze with composition $K_{0.23}TiO_2$ exhibiting hollandite structure (131 mAh g^{-1} at 20 mA g^{-1} and 67 mAh g^{-1} at 1000 mA g^{-1}). [29] Surprisingly, the presence of large potassium ions in the tunnel space does not seem to inhibit the (de)insertion of sodium in the hollandite structure contrary to what we have observed in the micrometric bronze $K_{0.2}TiO_2$. However, these authors did not address whether this unexpected result was due to a dominant surface redox pseudocapacitance in the nanometric bronze.

3.3 Revisiting the structural effect of sodium insertion (in *operando* XRD and HRTEM)

Phase evolution upon sodium intercalation in TiO_2(H) was analyzed by *operando* X-ray diffraction. The unit cell parameters of the TiO_2(H) under *operando* conditions are a = 10.1697(2) Å, c = 2.9657(1) Å and V = 306.73(1) $Å^3$ in excellent agreement with TiO_2(H) analyzed in ex situ conditions and with previous reports. [27] After a certain solid solution range of initial TiO_2(H) ($0 \leq x \leq 0.12$), the tetragonal *I*4/*m* phase reduced the symmetry to monoclinic (Fig. 5 a and b). This range is labeled A in Fig. 5 c. The region corresponding to the coexistence of the tetragonal and monoclinic phases is relatively narrow. Absence of a pronounced phase transitions during discharge and charge of TiO_2(H) is confirmed, although the splitting of 110, 200 and 310 tetragonal reflections caused by the monoclinic distortion is clearly observed in Fig. 5 b. After the tetragonal - monoclinic phase transition, Na_xTiO_2(H) exhibits a range of solid solution ($0.18 \leq x \leq 0.3$, labelled B in Fig. 5 c) after which a very closely related monoclinic phase is formed until the end of discharge is reached (x=0.47, labelled C in Fig. 5 c). Notably, this second monoclinic phase has not been observed so far. The *operando* X-ray diffraction patterns of the Na-containing phase after the phase transition were indexed in monoclinic space group *I*2/*m*, according to previously published theoretical and experimental results. [27, 28] The unit cell parameters of monoclinic Na_xTiO_2 for x=0.18 (labelled B) are a = 10.541(1) Å, b = 2.9702(6) Å, c= 9.9030(8) Å, β = 90.90(1)º and V = 309.78(4) $Å^3$ while for x=0.47 (labelled C) a = 10.746(2) Å, b = 2.9704(5) Å, c= 9.726(1) Å, β = 90.72(2)º and V = 310.4(1) $Å^3$. The unit cell parameters are not monotonous during sodiation and desodiation, and

phase transition from tetragonal to monoclinic symmetry is proved to be reversible (Fig. 5 b). Reversibility is nicely illustrated in Fig. S5 for the first two complete discharge-charge cycles. The regions with continuous shifts of the peak positions can be ascribed to solid solutions for the most part of the E-x curve (slopy profiles), while narrow compositional range of the E-x curve at approximately 1.15 V, can be associated with the tetragonal - monoclinic transformation of the unit cell with a relatively narrow coexistence of phases. It must be noted that upon Na^+ intercalation, the overall volume change was negligible and estimated as low as ~ 1% at a completely intercalated state after first discharge.

The Na_xTiO_2(H) formed upon discharge demonstrates a high crystallinity as evidenced from Fig. 5b. Detailed analysis by HRTEM in Fig. 6a - c shows that the ordered lattice fringes with spacings of 0.72 nm, 0.52 nm, and 0.49 nm, respectively, coincide with the (-101), (200) and (002) planes of monoclinic Na_xTiO_2(H). Specifically, the unequal spacings of (200) and (002) are a clear signature for the monoclinic distortion, because these reflections must have identical spacings in tetragonal symmetry. After charging, a unique value of 0.506 nm is found in desodiated TiO_2(H) for the (200) plane (Fig. 6e). In general, the ordered lattice fringes with spacings 0.71 nm, 0.506 nm and 0.32 nm, corresponding to the (110), (200) and (130) planes (Fig. 6 d-f), respectively, of tetragonal TiO_2(H) suggest that high crystallization of the product is maintained after complete removal of Na^+. These observations are in full agreement with the results of *operando* XRD analysis.

.

3.4 Electrochemical Impedance Spectroscopy

We have used Electrochemical Impedance Spectroscopy to determine both the sodium diffusion coefficient and the change in cell resistance upon long cycling. The impedance of a two-electrode cell was measured before the first discharge and after 80 cycles. The experimental data (dots) shown in Nyquist plots of Fig. 7 have been fitted to the equivalent circuit shown in the upper part of the figure. Cell impedance comprises not only the impedance of the working

electrode but also of the counter electrode. Thus, if sodium/electrolyte interface impedance is not negligible in the whole frequency range it cannot be used to extract information about some of the physicochemical processes of the working electrode (cathode-electrolyte interface resistance or charge-transfer resistance for instance). Fig. S6 of SI shows variation of imaginary part of impedance versus frequency measured in a three-electrode cell. Thus, the impedance of working electrode/electrolyte interface (-Im), counter electrode/electrolyte interface -Im(ce) can be separated. Impedance of working plus counter electrode -Im (we-ce) is also plotted. Impedance of the counter electrode at low frequencies is several orders of magnitude lower than that of the working electrode, which means that response of the two-electrode cell (Fig. 7) is dominated by the working electrode at low frequency. Therefore, the corresponding Warburg coefficient and hence, sodium diffusion coefficient can be determined. At higher frequency still interesting information can be extracted regarding how the total cell resistance varies upon cycling and therefore, the effect of aging on cell polarization and hence, on capacity decay.

The resistance R1, related to cell components, remains constant (ca. 5 ohm), while total resistance due to SEI and charge transfer resistances increase from 180 Ω to 600 Ω after 80 cycles. Thus, aging contributes to the increase in cell polarization and causes the slight but progressive decrease in capacity. In the low frequency region spikes are observed in both cases. Interestingly, in the case of the cycled electrode the spike observed at high frequencies fulfills the relationship expected for diffusion under semi-infinite linear conditions (-Im(Z) = Re(Z)). This condition is likely due to low diffusivity or to short diffusion depth when compared with particle size. On the other hand, that condition is also fulfilled for the initial non-cycled electrode but in a narrower frequency range. Charge accumulation on the surface of big particles (modelled as a capacitance [43-45]) could explain the observed deviation from 45º in the case of the non-cycled electrode. As electrochemical milling progresses, intercalation becomes more favored since the specific surface increases and accumulation of charge is minimized.

Diffusion coefficient of TiO_2(H) was only determined for the pristine non-cycled compound because specific area is known here. However once electrochemical milling takes place, the new specific surface could not be determined. Warburg coefficient, A_w in Eq. 1, has been determined

graphically by reading the minimum of $-Im(Z)*f^{1/2}$ versus f (Fig. S7 of SI). At this minimum, the Warburg diffusion process is the only contribution to EIS data. [46] Eq. 1 provides a sodium ion diffusion coefficient in TiO_2(H) of $2.6 \cdot 10^{-13}$ cm^2 s^{-1}. This is the first report of an experimental sodium ion diffusion coefficient in TiO_2(H) to the best of our knowledge. The diffusion coefficient of Na_xTiO_2 hollandite at room temperature was previously estimated theoretically from activation energy calculations. [28] At the dilute limit a very wide margin was found, ranging from $9.65 \cdot 10^{-6}$ cm^2 s^{-1} to $4.2 \cdot 10^{-9}$ cm^2 s^{-1} decreasing to $3.8 \cdot 10^{-15}$ cm^2 s^{-1} at higher concentration (x=0.31). However, the presence of defects in the 1-D diffusion tunnels is expected to lower the calculated diffusion coefficients, [28] as it can be the case of the experimental value reported in the present work. This situation reinforces the validity of our approach towards a fully potassium free sample to minimize this effect.

On the other hand, when comparing our experimental diffusion coefficient with those of other TiO_2 polymorphs determined by the same procedure (EIS) (rutile $1.37 \cdot 10^{-19}$ cm^2 s^{-1} [47], niobium doped rutile $4.31 \cdot 10^{-13}$ cm^2 s^{-1} [48], carbon coated hierarchical nanoporous TiO_2 microfibers $7.5 \cdot 10^{-15}$ cm^2 s^{-1} [49] or anatase ranging between $1.0 \cdot 10^{-11}$ to $17.6 \cdot 10^{-15}$ cm^2 s^{-1} as listed in the SI of ref. [50]), hollandite can be considered a kinetically very favored polymorph.

3.5 Diffusion- and surface-controlled contributions to specific capacity

When assessing the electrochemical performance of titanium oxides, besides diffusion-controlled intercalation the possible contribution of capacitive processes due to either surface redox or intercalation pseudocapacitance needs to be determined. If metal ion diffusion coefficient is low, the coexistence of both pseudocapacitive and diffusion controlled faradic processes may be an advantage, since both together provide high capacity. The former, in addition, may play the role of charge storage reservoir at high current rate. This is the case of nanosized TiO_2 rutile versus metallic lithium, able to sustain 70 mAh g^{-1} at 30 C [16], for which contribution to capacity at high current is dominated by surface storage. [20] Although TiO_2(H)

in this work is not initially nanosized and contribution of surface redox pseudocapacitance may be small, it can increase significantly upon electrochemical milling as is the case for other nanosized titanium dioxides.

The following electrochemical features have been considered to assess the participation of different physicochemical processes to charge storage: ac impedance experiment, shape of the cyclic voltammetry and the voltage vs capacity profile [51-53]. First, the presence of a spike in the impedance spectra shown in Fig. 7 supports the existence of diffusion-controlled charge storage. Regarding the shape of cyclic voltammetry, Fig. 8 shows data obtained at sweep rates from 1.2 to 0.03 mV s^{-1} once the cell was cycled several times at 1.5 mV s^{-1} to form the SEI. For the sake of clarity, they have been separated into two different graphs (Fig 8a and b); one at low scan rates (0.06-0.03 mV s^{-1}) and the other at higher scan rates (1.2-0.3 mV s^{-1}). The lowest scan rates are preferred for the analysis because they allow the presence of slow processes such as those controlled by semi-infinite diffusion to be enhanced. Voltammograms show two cathodic and two anodic peaks, R1, R2 and O1 and O2, respectively.

Peak current can be used to qualitatively determine the kinetics of the charge storage mechanism using the relationship $I = a\nu^b$ [54] where I is the measured current intensity at the cathodic and anodic peaks and ν the sweep rate. For capacitive processes, including pseudocapacitive ones, parameter b equals 1 whereas it equals 0.5 for diffusion controlled faradic processes [52, 55]. Fig. 8 c and d show the linear dependence of log (*I, mV)* with log (ν, mVs^{-1}) for reduction peaks R1 and R2. The slope b is very close to 0.5 indicating that both redox processes are diffusion controlled due to sodium intercalation into the bulk. The same conclusion is obtained for the oxidation peaks O1 and O2. Observing the shape of the voltammograms at low voltage, in which peaks R2 and O2 are clearly superimposed over a "box like" profile, it can be concluded that surface redox pseudocapacitive processes also participate in the charge storage likely with sodium ions being electrochemically absorbed at or near the surface [52, 56]. Interestingly, the behavior of the bronze $K_{0.2}TiO_2$, with the tunnel occupied by potassium, is slightly different. Fig. S8 of SI shows the CV profile of both TiO_2(H)

and the bronze $K_{0.2}TiO_2$. In the latter, broader peaks embedded in a clear "box like" profile point to a pseudocapacitive behavior [51-53]. In view of the high occupancy of the tunnel rapid diffusion in and out of the tunnel is discarded, and the pseudocapacitive contribution is ascribed to surface redox process. The developed capacity is poor (see Fig. S4 of SI) because of the low surface (micrometric crystals as seen in Fig. S3 of SI). Interestingly a high capacity similar to that of potassium-free hollandite has been reported for nanosized $K_{0.2}TiO_2$ bronze [9]. The similarity in CVs of both nanosized [9] and micrometric bronze in this work as well, as the very significant difference in capacity demonstrate the hindrance of sodium intercalation into the tunnel owed to the high potassium content. It plays a clear role in the contribution of the different physicochemical processes, i.e. diffusion-controlled faradic and surface redox pseudocapacitance, to total charge storage.

The voltage profile of TiO_2 hollandite (Fig. 2a) is not the typical for battery-like materials where a two-phase transformation gives rise to a constant voltage region or plateau. [53] The very narrow compositional range of the two-phase transformation and the existence of several solid solution regions (see Section 3.3) produce a mainly slopy voltage profile in TiO_2(H). However, due to sluggish sodium diffusion solid solutions do not give rise to intercalation pseudocapacitance but to surface-controlled pseudocapacitance besides diffusion-controlled faradic charge storage.

Cyclic voltammetry experiments at different sweep rates were recorded to determine the contribution of the diffusion-controlled faradic and surface-controlled pseudocapacitive processes. The contribution of the two storage mechanisms at each potential, a_1 and a_2 in I (V) = $a_1\nu + a_2\nu^{1/2}$, can be determined in the investigated voltage range. Details on the calculation procedure can be found in [57, 58].

A cell was cycled at decreasing scan rates, from 1.5 to 0.03 mV s^{-1}, in the 2.5 - 0.0 V voltage range. The linear dependence of $I/\nu^{1/2}$ vs $\nu^{1/2}$ is shown in Fig. S9 of SI. Plots of $I/\nu^{1/2}$ vs $\nu^{1/2}$ for selected potentials exemplify how a_1 and a_2 can be calculated from the straight lines obtained. Voltammograms conducted at very fast rate (1.2 mV s^{-1}) and very slow rate (0.03 mV

s^{-1}) showing the contribution of the two charge storage mechanisms are depicted in Fig. 9a and b, respectively, as examples. The black area accounts for the current corresponding to capacitive contribution, ascribed to surface redox pseudocapacitance, whereas the blue contour encloses the total current. The difference between the two areas accounts for the diffusion-controlled faradic contribution originated from mass diffusion. The data obtained from each sweep rate are depicted in Fig. 9c as a bar plot, clearly showing the variation of both contributions to total capacity at different sweep rates. As expected for an intercalation electrode with limited diffusion (owing to a low diffusion coefficient) throughout the bulk, the faster the scan rate the lower the diffusive contribution. Remarkably, only at very high sweep rate the capacitive contribution exceeds the diffusive one. In consideration of the low diffusion coefficient this means the surface is not high enough to largely contribute in contrast to other related cases [29]. Note that particle size could not even be reduced below 200 nm by means of electrochemical milling. Our results demonstrate that the good rate performance of TiO_2(H) at high sweep rate is due to both surface redox (pseudocapacitive) and diffusive (faradic bulk intercalation) storage processes. Interestingly, mass diffusion is still very significant at high sweep rate when compared with other TiO_2 polymorphs. This is attributed to better sodium diffusion in TiO_2(H), owing to its open tunnel structure enabling continuous but small variation of unit cell parameters upon almost the whole Na^+ (de)insertion process and sites available for Na^+ ions.

4. Conclusions

Potassium-free hollandite TiO_2(H), synthesized by oxidation of hollandite-type $K_{0.2}TiO_2$ bronze, is proposed as high-capacity electrode for sodium storage, and significant improvements in capacity and C-rate behavior have been achieved with respect to the parent $K_{0.2}TiO_2$ bronze. TiO_2(H) sustains a stable capacity of 106 mAh g^{-1} after 300 cycles at C/8 (42 mA g^{-1}) with a decrease of only 5.5% after 600 cycles. At high current (2C, 671 mA g^{-1}) 55 mAh g^{-1} are

maintained. Increase of cell resistance, observed after 80 cycles, contributes to loss of capacity as inferred from Impedance Spectroscopy.

Electrochemical features indicate that TiO_2(H) is a material with diffusion-limited kinetics. However, the voltage profile shows signature of a pseudocapacitive behavior rather than the commonly observed constant voltage profile of typical battery materials. [53] A very narrow compositional range of the two-phase transformation and the existence of several solid solution regions produce a mainly slopy voltage profile in TiO_2(H). However, due to sluggish sodium diffusion solid solutions do not give rise to intercalation pseudocapacitance but to surface-controlled pseudocapacitance, besides diffusion-controlled faradic charge storage (intercalation into the tunnel). Cyclic voltammetry revealed contribution of pseudocapacitive processes over a wide voltage range, however, significant contribution of diffusive process even at high current is confirmed.

In this work we revealed some unique properties of TiO_2(H). While most other TiO_2 polymorphs exhibit extrinsic pseudocapacitive behavior due to very low diffusion coefficients, hollandite TiO_2(H) behaves as sodium battery electrode material with significant participation of diffusion-controlled faradic process and surface redox pseudocapacitance in a wide voltage range. The latter is likely favored by the still low sodium ion diffusion coefficient of TiO_2(H), 2.6 10^{-13} cm^2 s^{-1}. Nevertheless, $D_{(Na+)}$ of TiO_2(H) is several orders of magnitude higher than those of anatase and most of reported rutiles, pointing to hollandite as one of the most promising polymorphs for the development of TiO_2-based sodium ion anodes. Further reducing the particle size to the scale of a few nanometers may largely improve the electrochemical performance of TiO_2(H) due to enhanced contribution of surface redox pseudocapacitance.

5. Acknowledgements

We thank “MCIN/ AEI /10.13039/501100011033 and Fondo Europeo de Desarrollo Regional” (FEDER/UE) for funding the project PID2019-106662RB-C41. Financial support from

Universidad San Pablo is also acknowledged. Authors are also very grateful to the BioNanoTechno Center of University of Bialystok for granting access to its facilities financed by the EU funds (Nos. POPW.01.03.00-20.034/09-00 and POPW.01.03.00-20-004/11-00) and for technical support. ADC thanks Fundación Universitaria San Pablo CEU for the grant "Ayudas a la Movilidad CEINDO-Santander" allowing the stay in the Department of Physical Chemistry, Group of Materials Chemistry, University of Bialystok.

6. References

[1] K. Zaghib, M. Simoneau, M. Armand, M. Gauthier, Electrochemical study of Li4Ti5O12 as negative electrode for Li-ion polymer rechargeable batteries, Journal of Power Sources, 81 (1999) 300-305.
[2] J.Y. Liao, V. Chabot, M. Gu, C.M. Wang, X.C. Xiao, Z.W. Chen, Dual phase Li4Ti5O12-TiO2 nanowire arrays as integrated anodes for high-rate lithium-ion batteries, Nano Energy, 9 (2014) 383-391.
[3] T.F. Yi, T.T. Wei, Y. Li, Y.B. He, Z.B. Wang, Efforts on enhancing the Li-ion diffusion coefficient and electronic conductivity of titanate-based anode materials for advanced Li-ion batteries, Energy Storage Materials, 26 (2020) 165-197.
[4] Y.T. Zhao, S.Y. Nong, C.L. Dong, M.Y. Chen, S. Liang, M.Z. Cai, F.Q. Huang, p "Quasi-Zero-Strain" TiO2-x as an Ultra-Long-Life Anode for Li-Ion Batteries, Acs Applied Energy Materials.
[5] Y. Sun, L. Zhao, H. Pan, X. Lu, L. Gu, Y.-S. Hu, H. Li, M. Armand, Y. Ikuhara, L. Chen, X. Huang, Direct atomic-scale confirmation of three-phase storage mechanism in Li4Ti5O12 anodes for room-temperature sodium-ion batteries, Nature Communications, 4 (2013) 1870.
[6] L. Zhao, H.L. Pan, Y.S. Hu, H. Li, L.Q. Chen, Spinel lithium titanate (Li4Ti5O12) as novel anode material for room-temperature sodium-ion battery, Chinese Physics B, 21 (2012).
[7] M. Gutierrez-Florez, A. Kuhn, F. Garcia-Alvarado, Electrochemical lithium intercalation in K1.2Ti8O16 and synthesis of new bronzes K1.2-xTi8O16, Boletin De La Sociedad Espanola De Ceramica Y Vidrio, 37 (1998) 260-263.
[8] M.T. Gutierrez-Florez, A. Kuhn, F. Garcia-Alvarado, Lithium intercalation in KxTi8O16 compounds, International Journal of Inorganic Materials, 1 (1999) 117-121.
[9] D. Li, W. Guo, Y. Li, Y. Tang, J. Yan, X. Meng, M. Xia, F. Gao, Tunnel structured hollandite K0.06TiO2 microrods as the negative electrode for 2.4 V flexible all-solid-state asymmetric supercapacitors with high performance, Journal of Power Sources, 413 (2019) 34-41.
[10] L.D. Noailles, C.S. Johnson, J.T. Vaughey, M.M. Thackeray, Lithium insertion into hollandite-type TiO2, Journal of Power Sources, 81 (1999) 259-263.
[11] M. Sakao, N. Kijima, J. Akimoto, T. Okutani, Synthesis, crystal structure, and electrochemical properties of hollandite-type K0.008TiO2, Solid State Ionics, 225 (2012) 502-505.
[12] M. Sakao, N. Kijima, J. Akimoto, T. Okutani, Lithium insertion and extraction properties of hollandite-type KxTiO2 with different K content in the tunnel space, Solid State Ionics, 243 (2013) 22-29.
[13] T. Ohzuku, T. Kodama, T. Hirai, Electrochemistry of anatase titanium dioxide in lithium nonaqueous cells, J. Power Sources, 14 (1985) 153-166.

[14] D.W. Murphy, F.J. Di Salvo, J.N. Carides, J.V. Waszczak, Topochemical reactions of rutile related structures with lithium, Materials Research Bulletin, 13 (1978) 1395-1402.
[15] T. Ohzuku, Z. Takehara, S. Yoshizawa, NON-AQUEOUS LITHIUM-TITANIUM DIOXIDE CELL, Electrochimica Acta, 24 (1979) 219-222.
[16] Y.-S. Hu, L. Kienle, Y.-G. Guo, J. Maier, High lithium electroactivity of nanometer-sized rutile TiO2, Advanced Materials, 18 (2006) 1421-1426.
[17] A. Kuhn, R. Amandi, F. García-Alvarado, Electrochemical lithium insertion in TiO2 with the ramsdellite structure, J. Power Sources, 92 (2001) 221-227.
[18] M.A. Reddy, V. Pralong, U.V. Varadaraju, B. Raveau, Crystallite size constraints on lithium insertion into brookite TiO(2), Electrochemical and Solid State Letters, 11 (2008) A132-A134.
[19] A.R. Armstrong, G. Armstrong, J. Canales, R. Garcia, P.G. Bruce, Lithium-ion intercalation into TiO2-B nanowires, Advanced Materials, 17 (2005) 862-+.
[20] P. Díaz-Carrasco, A. Duarte-Cárdenas, A. Kuhn, F. García-Alvarado, Understanding the high performance of nanosized rutile TiO2 anode for lithium-ion batteries, Journal of Power Sources, 515 (2021) 230632.
[21] Z.-G. Liu, R. Du, X.-X. He, J.-C. Wang, Y. Qiao, L. Li, S.-L. Chou, Recent Progress on Intercalation-Based Anode Materials for Low-Cost Sodium-Ion Batteries, ChemSusChem, 14 (2021) 3724-3743.
[22] K.-T. Kim, G. Ali, K.Y. Chung, C.S. Yoon, H. Yashiro, Y.-K. Sun, J. Lu, K. Amine, S.-T. Myung, Anatase Titania Nanorods as an Intercalation Anode Material for Rechargeable Sodium Batteries, Nano Letters, 14 (2014) 416-422.
[23] D. Su, S. Dou, G. Wang, Anatase TiO2: Better Anode Material Than Amorphous and Rutile Phases of TiO2 for Na-Ion Batteries, Chemistry of Materials, 27 (2015) 6022-6029.
[24] H. Usui, S. Yoshioka, K. Wasada, M. Shimizu, H. Sakaguchi, Nb-Doped Rutile TiO2: a Potential Anode Material for Na-Ion Battery, Acs Applied Materials & Interfaces, 7 (2015) 6567-6573.
[25] J.P. Huang, D.D. Yuan, H.Z. Zhang, Y.L. Cao, G.R. Li, H.X. Yang, X.P. Gao, Electrochemical sodium storage of TiO2(B) nanotubes for sodium ion batteries, RSC Advances, 3 (2013) 12593-12597.
[26] R.D. Shannon, C.T. Prewitt, EFFECTIVE IONIC RADII IN OXIDES AND FLUORIDES, Acta Crystallographica Section B-Structural Crystallography and Crystal Chemistry, B 25 (1969) 925-&.
[27] J.C. Perez-Flores, C. Baehtz, A. Kuhn, F. Garcia-Alvarado, Hollandite-type TiO2: a new negative electrode material for sodium-ion batteries, Journal of Materials Chemistry A, 2 (2014) 1825-1833.
[28] A. Vasileiadis, M. Wagemaker, Thermodynamics and Kinetics of Na-Ion Insertion into Hollandite-TiO2 and O3-Layered NaTiO2: An Unexpected Link between Two Promising Anode Materials for Na-Ion Batteries, Chemistry of Materials, 29 (2017) 1076-1088.
[29] Q. Zhang, Y. Wei, H. Yang, D. Su, Y. Ma, H. Li, T. Zhai, Tunnel-Structured KxTiO2 Nanorods by in Situ Carbothermal Reduction as a Long Cycle and High Rate Anode for Sodium-Ion Batteries, ACS Applied Materials & Interfaces, 9 (2017) 7009-7016.
[30] J. Liu, J. Wang, C. Xu, H. Jiang, C. Li, L. Zhang, J. Lin, Z.X. Shen, Advanced Energy Storage Devices: Basic Principles, Analytical Methods, and Rational Materials Design, Advanced Science, 5 (2018) 1700322.
[31] M. Watanabe, Y. Komatsu, T. Sasaki, Y. Fujiki, A new oxidation process of potassium titanium dioxide bronze with the hollandite structure, Journal of Solid State Chemistry, 92 (1991) 80-87.
[32] M. Latroche, L. Brohan, R. Marchand, M. Tournoux, New hollandite oxides: TiO2(H) and K0.06TiO2, Journal of Solid State Chemistry, 81 (1989) 78-82.
[33] J. Rodríguez-Carvajal, Recent advances in magnetic structure determination by neutron powder diffraction, Physica B: Condensed Matter, 192 (1993) 55-69.
[34] J.B. Leriche, S. Hamelet, J. Shu, M. Morcrette, C. Masquelier, G. Ouvrard, M. Zerrouki, P. Soudan, S. Belin, E. Elkaïm, F. Baudelet, An Electrochemical Cell for Operando Study of

Lithium Batteries Using Synchrotron Radiation, Journal of The Electrochemical Society, 157 (2010) A606.
[35] W. Weppner, R.A. Huggins, Determination of the Kinetic Parameters of Mixed-Conducting Electrodes and Application to the System Li3Sb, Journal of The Electrochemical Society, 124 (1977) 1569-1578.
[36] C. Ho, I.D. Raistrick, R.A. Huggins, Application of AC techniques to the study of lithium difussion in tungsten trioxide thin-films Journal of the Electrochemical Society, 127 (1980) 343-350.
[37] N. Kijima, M. Sakao, T. Manabe, J. Akimoto, Synthesis, crystal structure, and electrochemical properties of niobium-substituted hollandite-type titanium dioxides, KxTi1-yNbyO2, with different potassium content in the tunnel space, Solid State Ionics, 369 (2021).
[38] J.-T. Han, Y.-H. Huang, J.B. Goodenough, New Anode Framework for Rechargeable Lithium Batteries, Chemistry of Materials, 23 (2011) 2027-2029.
[39] H. Song, Y.-T. Kim, A Mo-doped TiNb2O7 anode for lithium-ion batteries with high rate capability due to charge redistribution, Chemical Communications, 51 (2015) 9849-9852.
[40] H. Li, L. Shen, G. Pang, S. Fang, H. Luo, K. Yang, X. Zhang, TiNb2O7 nanoparticles assembled into hierarchical microspheres as high-rate capability and long-cycle-life anode materials for lithium ion batteries, Nanoscale, 7 (2015) 619-624.
[41] R. Inada, T. Mori, R. Kumasaka, R. Ito, T. Tojo, Y. Sakurai, Characterization of vacuum-annealed TiNb2O7 as high potential anode material for lithium-ion battery, International Journal of Applied Ceramic Technology, 16 (2019) 264-272.
[42] A. Rudola, K. Saravanan, S. Devaraj, H. Gong, P. Balaya, Na2Ti6O13: a potential anode for grid-storage sodium-ion batteries, Chemical Communications, 49 (2013) 7451-7453.
[43] D.J. Kim, R. Ponraj, A.G. Kannan, H.-W. Lee, R. Fathi, R. Ruffo, C.M. Mari, D.K. Kim, Diffusion behavior of sodium ions in Na0.44MnO2 in aqueous and non-aqueous electrolytes, Journal of Power Sources, 244 (2013) 758-763.
[44] M.D. Levi, G. Salitra, B. Markovsky, H. Teller, D. Aurbach, U. Heider, L. Heider, Solid-state electrochemical kinetics of Li-ion intercalation into Li1-xCoO2: Simultaneous application of electroanalytical techniques SSCV, PITT, and EIS, Journal of the Electrochemical Society, 146 (1999) 1279-1289.
[45] D. Andre, M. Meiler, K. Steiner, H. Walz, T. Soczka-Guth, D.U. Sauer, Characterization of high-power lithium-ion batteries by electrochemical impedance spectroscopy. II: Modelling, Journal of Power Sources, 196 (2011) 5349-5356.
[46] H. Anne, Understanding the kinetic limitations of NaFePO4 as cathode active material for Na-ion batteries, Universidad del País Vasco, 2019.
[47] S. Ghosh, V. Kiran Kumar, S.K. Kumar, S. Biswas, S.K. Martha, An insight of sodium-ion storage, diffusivity into TiO2 nanoparticles and practical realization to sodium-ion full cell, Electrochimica Acta, 316 (2019) 69-78.
[48] F. Zhao, B. Wang, Y. Tang, H. Ge, Z. Huang, H.K. Liu, Niobium doped anatase TiO2 as an effective anode material for sodium-ion batteries, Journal of Materials Chemistry A, 3 (2015) 22969-22974.
[49] N. Wang, Y. Gao, Y.-X. Wang, K. Liu, W. Lai, Y. Hu, Y. Zhao, S.-L. Chou, L. Jiang, Nanoengineering to Achieve High Sodium Storage: A Case Study of Carbon Coated Hierarchical Nanoporous TiO2 Microfibers, Advanced Science, 3 (2016) 1600013.
[50] X. Wang, L. Qi, H. Wang, Anatase TiO2 as a Na+-Storage Anode Active Material for Dual-Ion Batteries, ACS Applied Materials & Interfaces, 11 (2019) 30453-30459.
[51] V. Augustyn, P. Simon, B. Dunn, Pseudocapacitive oxide materials for high-rate electrochemical energy storage, Energy & Environmental Science, 7 (2014) 1597-1614.
[52] C. Choi, D.S. Ashby, D.M. Butts, R.H. DeBlock, Q. Wei, J. Lau, B. Dunn, Achieving high energy density and high power density with pseudocapacitive materials, Nature Reviews Materials, 5 (2020) 5-19.
[53] Y. Gogotsi, R.M. Penner, Energy Storage in Nanomaterials – Capacitive, Pseudocapacitive, or Battery-like?, ACS Nano, 12 (2018) 2081-2083.

[54] H. Lindström, S. Södergren, A. Solbrand, H. Rensmo, J. Hjelm, A. Hagfeldt, S.-E. Lindquist, Li+ Ion Insertion in TiO2 (Anatase). 2. Voltammetry on Nanoporous Films, The Journal of Physical Chemistry B, 101 (1997) 7717-7722.
[55] J. Wang, J. Polleux, J. Lim, B. Dunn, Pseudocapacitive Contributions to Electrochemical Energy Storage in TiO2 (Anatase) Nanoparticles, The Journal of Physical Chemistry C, 111 (2007) 14925-14931.
[56] J. Come, V. Augustyn, J.W. Kim, P. Rozier, P.-L. Taberna, P. Gogotsi, J.W. Long, B. Dunn, P. Simon, Electrochemical Kinetics of Nanostructured Nb₂O₅Electrodes, Journal of The Electrochemical Society, 161 (2014) A718-A725.
[57] M. Sathiya, A.S. Prakash, K. Ramesha, J.M. Tarascon, A.K. Shukla, V2O5-Anchored Carbon Nanotubes for Enhanced Electrochemical Energy Storage, Journal of the American Chemical Society, 133 (2011) 16291-16299.
[58] S. Rubio, R.R. Maça, M.J. Aragón, M. Cabello, M. Castillo-Rodríguez, P. Lavela, J.L. Tirado, V. Etacheri, G.F. Ortiz, Superior electrochemical performance of TiO2 sodium-ion battery anodes in diglyme-based electrolyte solution, J. Power Sources, 432 (2019) 82-91.

Figure captions.

Fig. 1 TEM images of $K_{0.20}TiO_2$ (a) and TiO_2(H) (b) rods. HRTEM images of $K_{0.20}TiO_2$ (c) and TiO_2(H) (d) projected along the same [-110] direction exhibiting characteristic (110) and (001) planes, together with its structural model in (d) viewed from the [-110] crystallographic direction. TiO_6: green octahedra, O: red spheres.

Fig. 2. a) Discharge-charge voltage profile for selected cycles of a sodium cell with TiO_2(H) as the active material of the positive electrode at C/8 rate (42 mA g^{-1}); b) Variation of capacity upon cycling and coulombic efficiency.

Fig 3. SEM images of: a) an as prepared electrode surface (before first discharge); b) after 100 cycles at C/20.

Fig. 4. Rate capability of TiO_2(H) as shown by the charge-discharge capacity variation under several rates ranging from C/20 to 2C.

Fig. 5. Results of *operando* X-ray diffraction experiment for Na^+ (de)intercalation in TiO_2(H). Evolution of XRD patterns (indexed in the initial *I*4/*m* tetragonal cell) (a); splitting of selected tetragonal (t) into monoclinic (m) reflections (b); waterfall plot of 200_t and 310_t reflections evidencing phase transitions upon sodiation of TiO_2(H) (c).

Fig. 6. HRTEM image of an TiO_2(H) electrode at different state of charge (SOC) in a Na battery. Sodiated Na_xTiO_2(H) at the fully discharged state at 0.01 V (a-c) and desodiated TiO_2(H) obtained at the charged state at 3.0 V (d-f). Voltages are expressed vs. Na^+/Na.

Fig. 7. Nyquist plot corresponding to TiO_2(H) // Na cell impedance (Experimental data: red and blue solid circles; solid line depicts the fitting to the equivalent circuit shown on top of plot.

Fig. 8. Cyclic voltammograms at a) 0.06-0.03 mV s^{-1} and b) 1.2-0.3 mV s^{-1} sweep rates; log (*I, mA) vs* log (ν, mV s^{-1}) linear dependence for peak current c) R1, d) R2, e) O1 and f) O2 . Accordingly to the slope of the straight line log $I = a + b \log \nu$, a faradic diffusion-controlled process (b=0.5) takes place at the corresponding voltages. (Correlation coefficient values for c-f *r* are: 0.997; 0.989; 0.997 ; 0.990 respectively.

Fig. 9. Cyclic voltammograms at a) 1.2 and b) 0.003 mV s^{-1} sweep rates and corresponding capacitive contributions (black area) to total capacity (area inside the blue contour); c) bar chart showing the contribution (%) of capacitive and diffusion-controlled processes to total capacity of TiO_2(H) as function of scan rate.

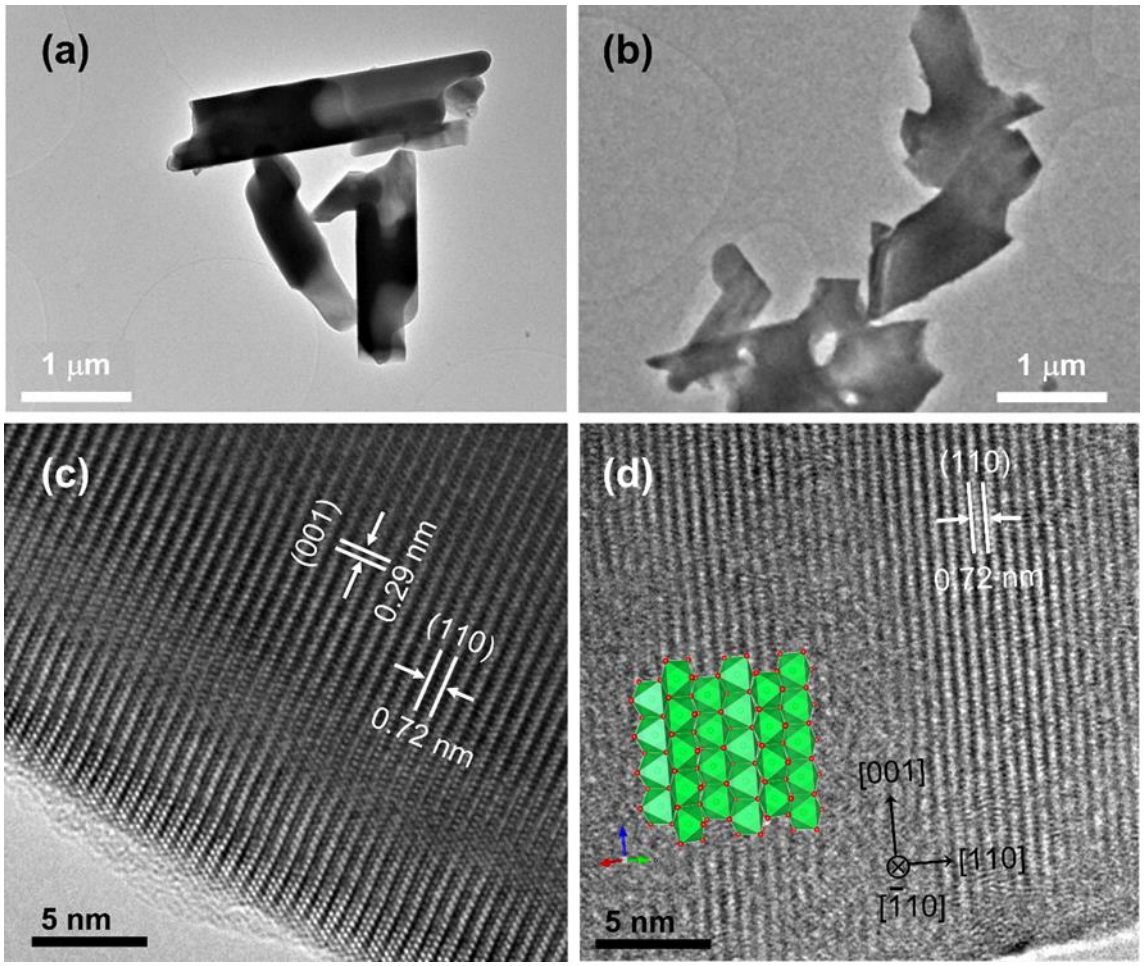

Figure 1. A. Duarte Cárdenas et al.

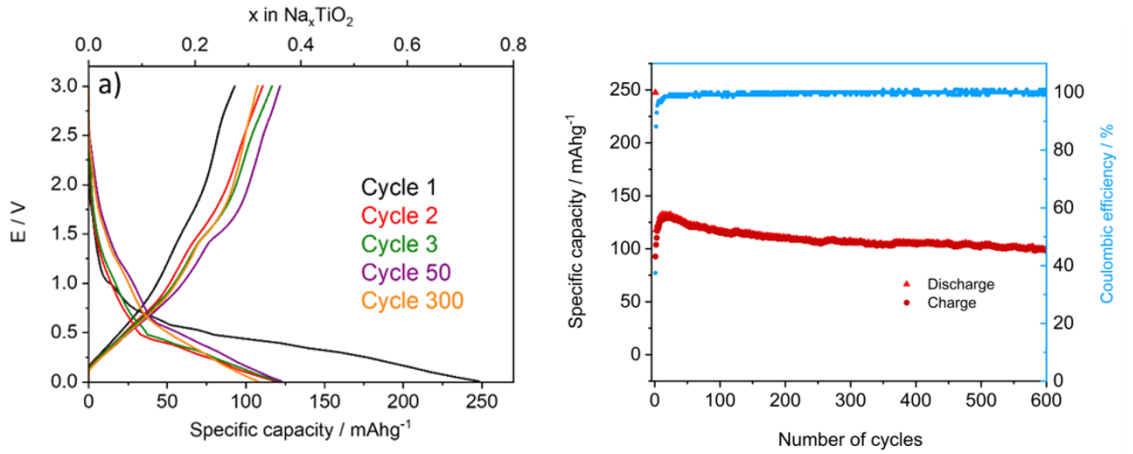

Figure 2. A. Duarte Cárdenas et al.

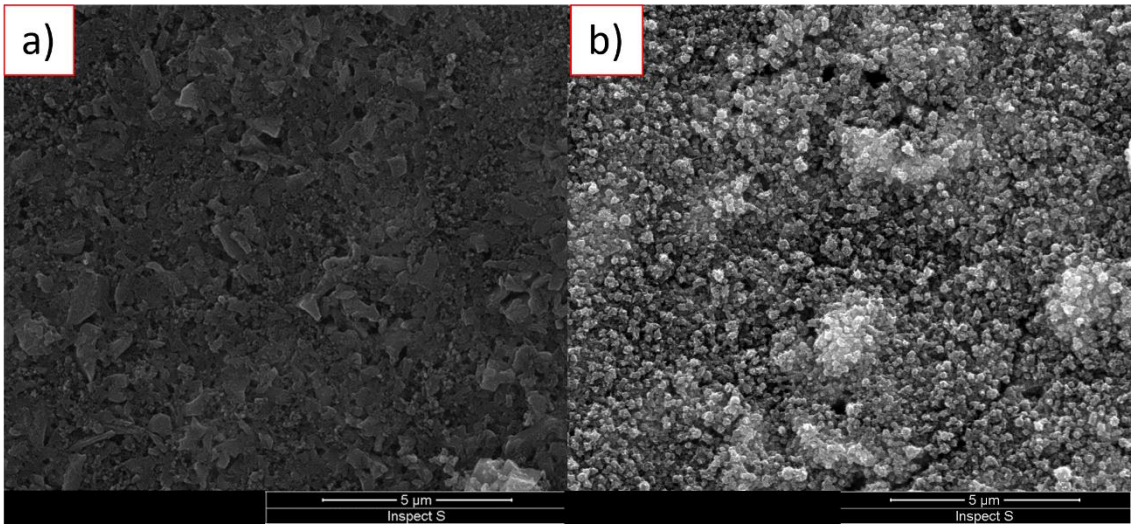

Figure 3. A. Duarte Cárdenas et al.

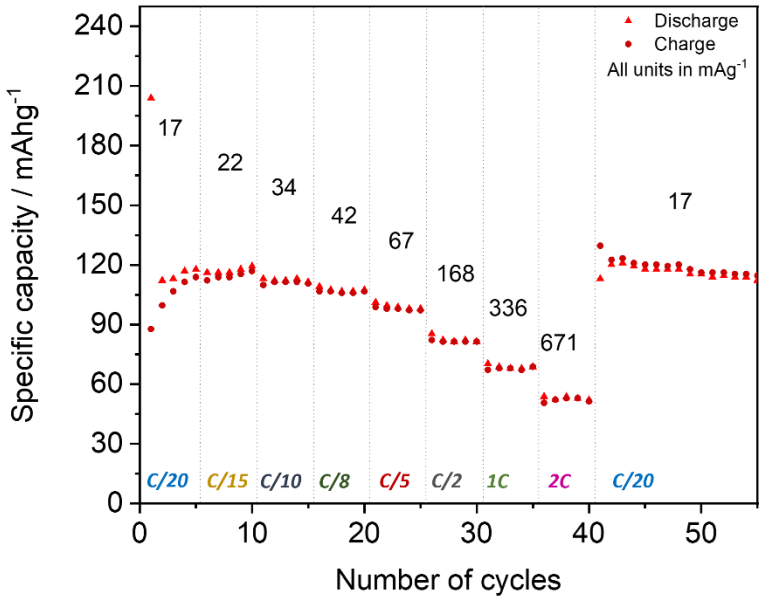

Figure 4. A. Duarte Cárdenas et al.

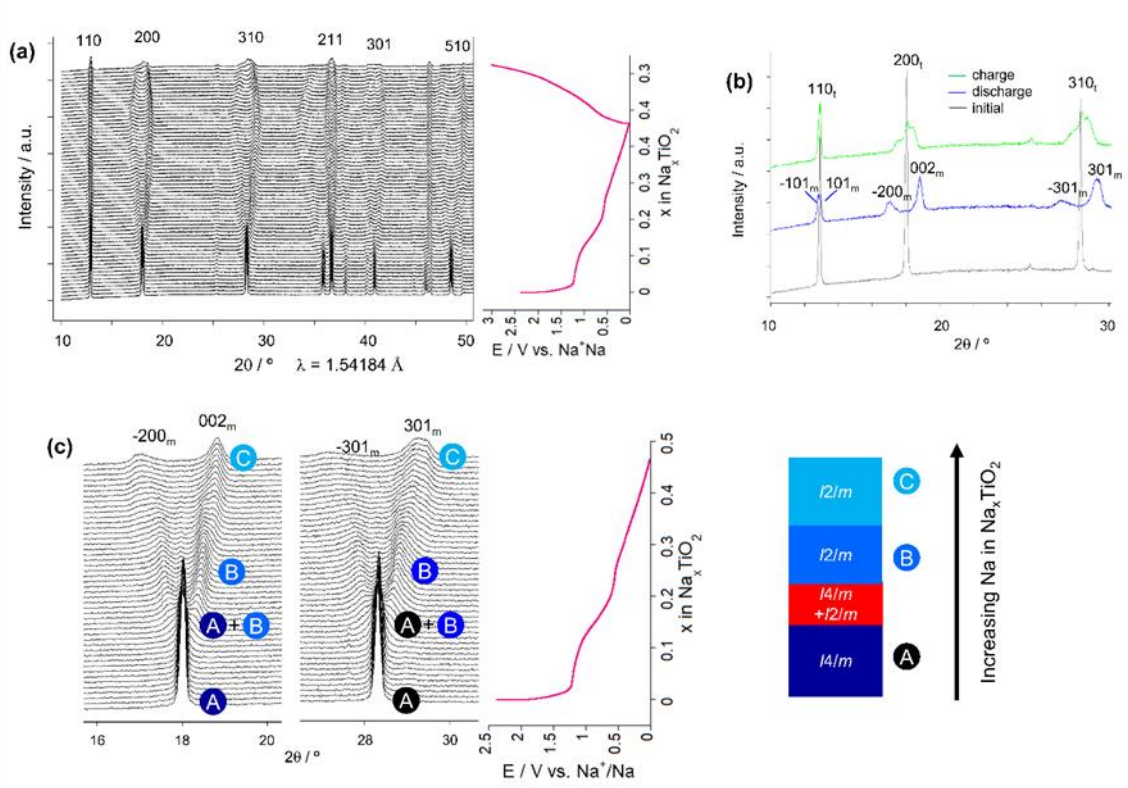

Figure 5. A. Duarte Cárdenas et al.

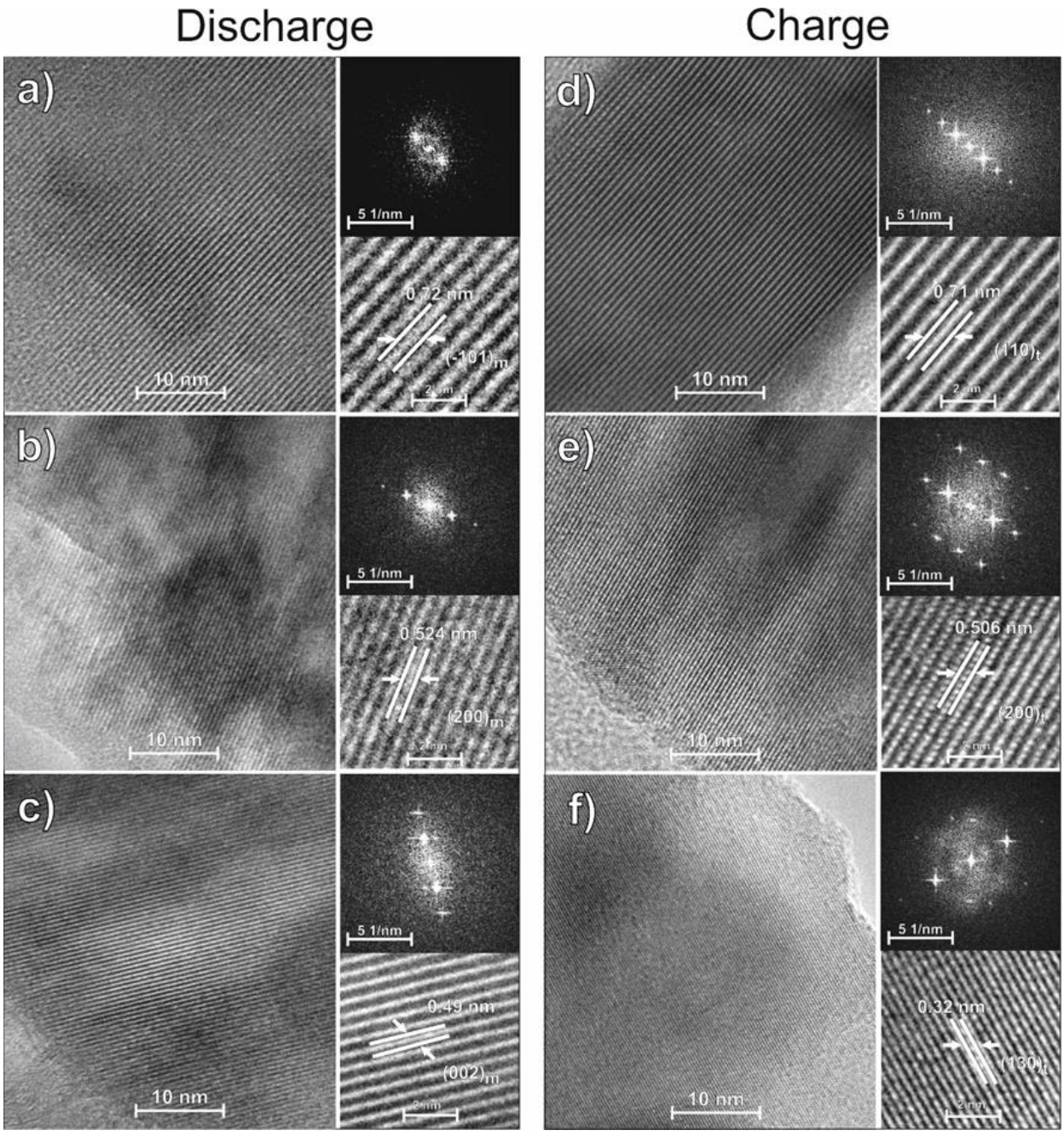

Figure 6. A. Duarte Cárdenas et al.

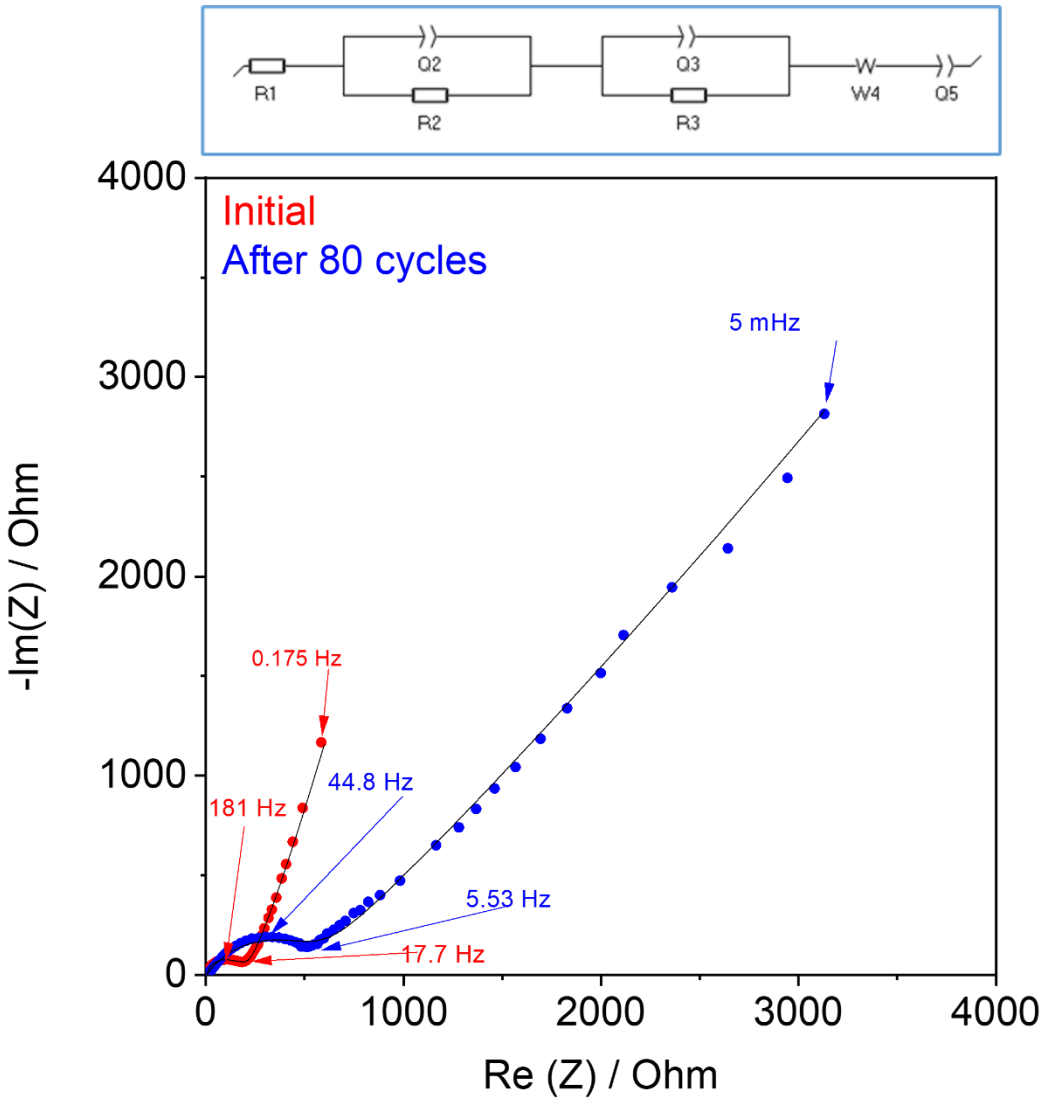

Figure 7. A. Duarte Cárdenas et al.

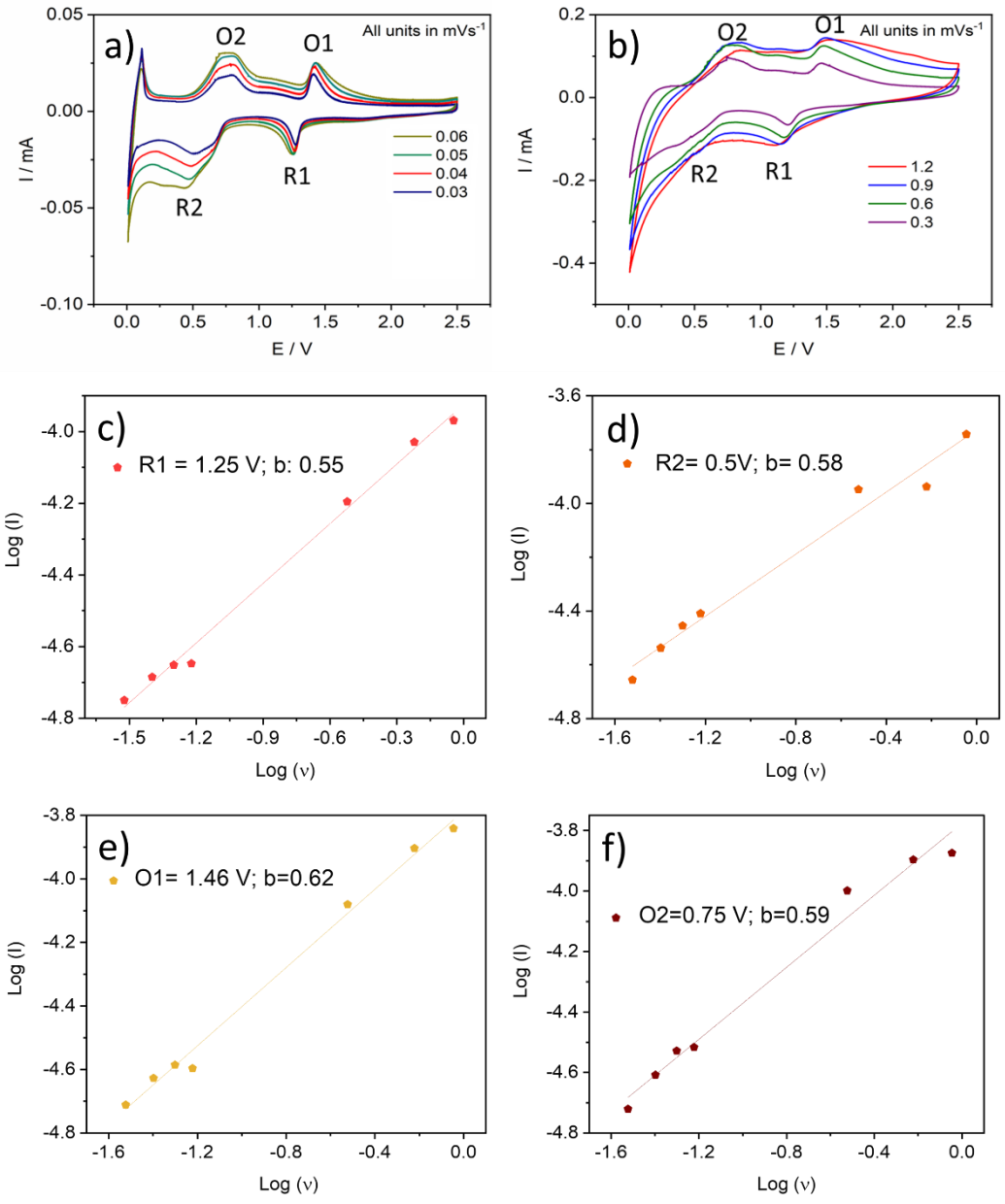

Figure 8. A. Duarte Cárdenas et al.

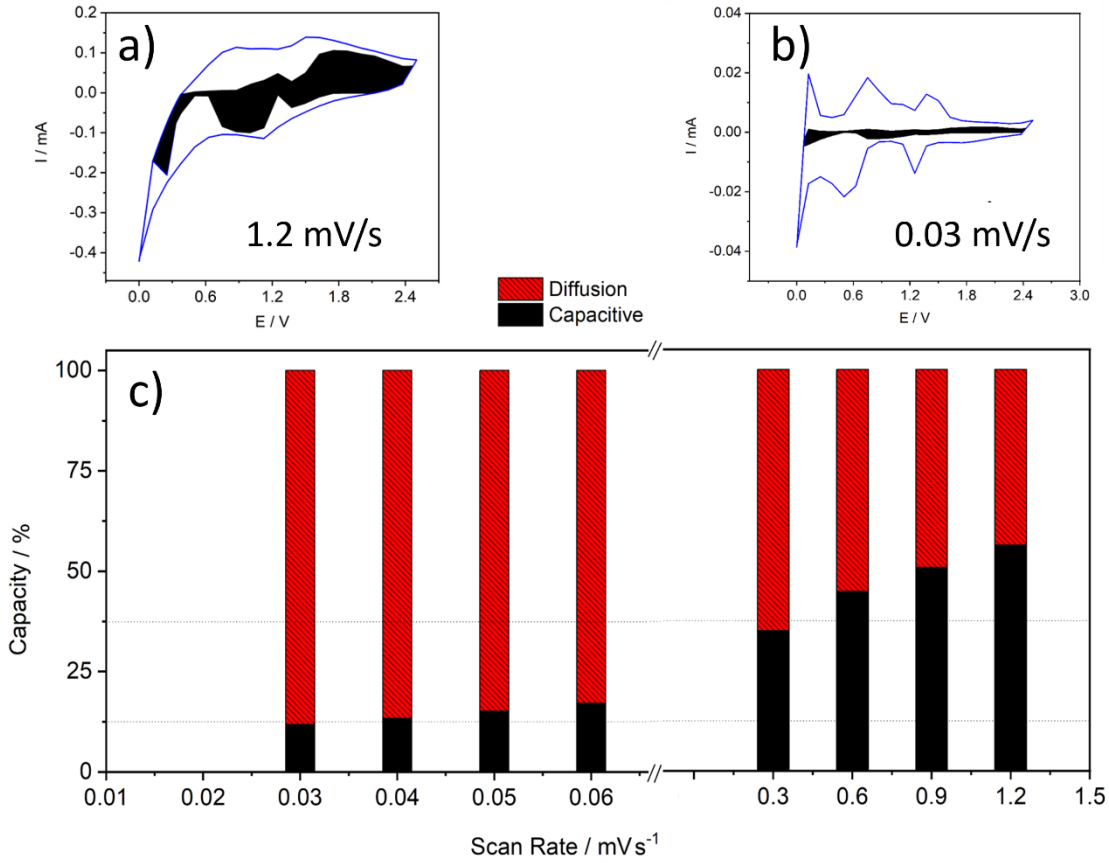

Figure 9. A. Duarte Cárdenas et al.